1 **Soil Organic Carbon Projections and Climate Adaptation Strategies across**

2 **Pacific Rim Agro-ecosystems**

4 Chien-Hui Syu[1], Chun-Chien Yen[1,2], Selly Maisyarah[2], Bo-Jiun Yang[1], Yu-Min Tzou[2], and

5 Shih-Hao Jien[2*]

6 [1] Agricultural Chemistry Division, Taiwan Agricultural Research Institute, Taichung City

7 40227, Taiwan, ROC

8 [2] Department of Soil and Environmental Sciences, National Chung Hsing University,

9 Taichung 40227, Taiwan, ROC

11 Corresponding author: Shih-Hao Jien; E-mail: shjien@nchu.edu.tw
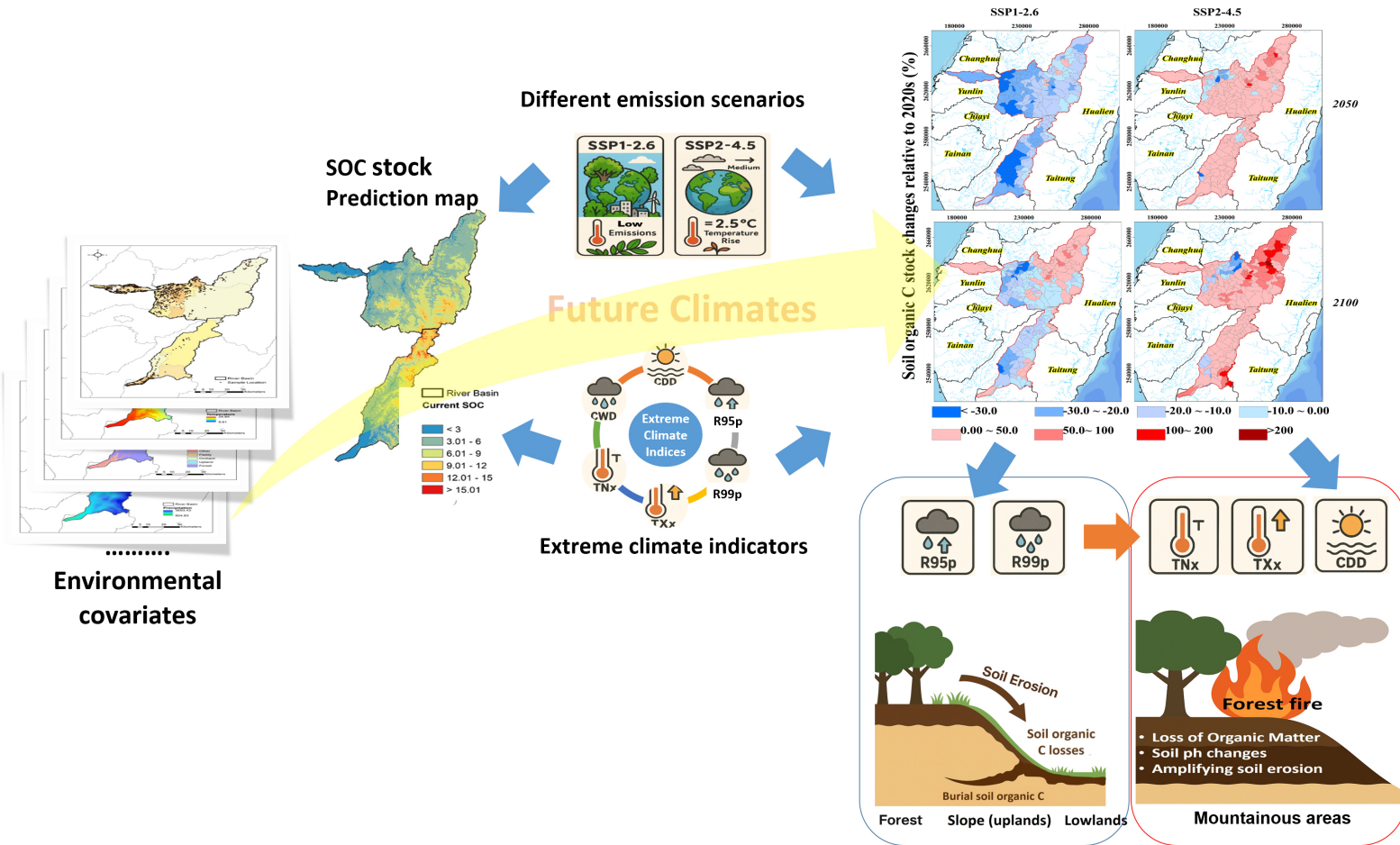
Abstract

In Pacific Rim regions highly exposed to climate variability, accurate projections of soil organic carbon (SOC) are critical for future effective land management and climate adaptation strategies. This study integrated digital soil mapping with CMIP6-based climate projections to estimate the spatiotemporal distribution of SOC stocks in subtropical (Zhuoshui River) and tropical (Laonong River) watersheds in Taiwan. We collected 901 soil samples and data on 18 environmental covariates and modeled SOC stocks at a 20-m resolution through the Cubist and random forest algorithms, which were also combined with regression kriging. The Cubist-based kriging model was discovered to achieve the highest performance in SOC stock prediction. Mountainous areas were found to contain >80% of SOC stocks, and tropical zones were discovered to store substantially less carbon than subtropical zones. Future emission scenarios revealed spatial heterogeneity in SOC stock dynamics. Under scenario SSP1-2.6, SOC stocks were projected to decline by up to 20.9%, especially in uplands, due to erosion driven by extreme rainfall (R95p, R99p). In contrast, scenario SSP2-4.5 predicted SOC stock increases of 7.9%, particularly in mountainous areas where higher TNx and TXx enhanced productivity. Partial least squares path modeling revealed a climate–topography interaction and explicitly quantified their contributions to SOC stocks, dominated by topography and followed by prolonged dry spells (CDD). This interaction is more pronounced in uplands than in mountainous areas, where topography mitigates temperature extremes and their effects on SOC stocks. Extended CDD may decrease organic inputs by reducing vegetation growth and soil moisture, thereby enhancing carbon losses. Examining the interactions between climatic extremes, landscape types, and SOC stocks is essential for enhancing soil resilience and ensuring stable SOC stocks in the future.

Keywords: soil organic carbon, stock, digital soil mapping, climatic extreme, emission scenario, land type

1. Introduction

Soil organic carbon (SOC) is one of the largest carbon pools in the global carbon cycle (Grace, 2004) and is a key concern of agricultural and environmental policies (Johnston et al., 2004). SOC also has a crucial influence on the carbon cycle at the local and global levels (Singh et al., 2018). Multiple studies have examined whether carbon storage in agricultural soils can offset global warming, and various frameworks have been developed for evaluating the dynamics of SOC. Among these, the landscape scale has enabled researchers to consider the interplay between natural processes, human patterns, and SOC dynamics (Viaud et al., 2010). Therefore, this scale is the most appropriate for assessing environmental and agricultural ecosystems (Li et al., 2021).

Changes in climatic conditions such as temperature, carbon dioxide concentration, and precipitation may influence the dynamics of SOC by affecting the rates of soil processes such as mineralization, decomposition, leaching, and total carbon loss. In areas prone to climatic extremes—such as floods, droughts, and heat waves—these conditions may further affect the dynamics of SOC (Li et al., 2021; Chalchissa et al., 2022). In addition, extreme climate events may strongly affect the content of SOC, with subsequent effects on agricultural productivity and ecosystem services. Therefore, before the dynamics of SOC can be evaluated at the landscape scale in response to climate change, a spatiotemporal technique is required. Zhu and Lin (2010) argued that in areas with major terrain variation and low sampling density, utilizing a non-geostatistical approach or a combination of geostatistical and non-geostatistical approaches can improve prediction ability.

In digital soil mapping (DSM), soil properties in unsampled areas are predicted using statistical or machine learning models that relate soil observations to environmental factors (Grunwald, 2009). Spatial variability is key to model construction (Zhu and Lin, 2010). There are two major approaches including: (1) non-geostatistical methods based on the SCORPAN model (Jenny, 1941; McBratney et al., 2003), such as multiple linear regression (MLR), generalized additive models, Cubist, and random forest (RF) (Quinlan, 1992; Breiman, 2001); and (2) geostatistical methods accounting for spatial autocorrelation, including ordinary, simple, and universal kriging. Machine learning algorithms (e.g., MLR, RF, Cubist) are widely applied for mapping SOC content and stocks (Lamichhane et al., 2019; Siewert, 2018; Rudiyanto et al., 2018). Model performance depends on spatial scale, observation density), and terrain (Zhu and Lin, 2010; Tsui et al., 2016; Keskin and Grunwald, 2018). This study used regression kriging, a hybrid approach combining regression models (e.g., Cubist, RF) with spatial interpolation of

76 residuals (Ma et al., 2017). Although regression kriging often improves RF and Cubist
77 predictions, its advantage is not universal, highlighting the need for meta-analytical evaluations
78 (Vaysse and Lagacherie, 2015; Ma et al., 2017; Lamichhane et al., 2019).

79   Taiwan is located on the frontline of the Pacific Rim and is highly prone to the combined
80 effects of climate change and El Niño–Southern Oscillation events. The frequency and spatial
81 variability of extreme climate events in this region are expected to dramatically increase in the
82 future. Therefore, understanding the combined effects of extreme climate variability and long-
83 term climate change on regional climate and SOC variation is essential for evaluating the
84 vulnerability of regional agriculture, water resources, and ecosystems. In Taiwan, the Zhuoshui
85 River Watershed (ZRW) and Laonong River Watershed (LRW) are the two largest and most
86 crucial agricultural eco-watersheds. The ZRW includes fluvial plains and is one of the most
87 essential agricultural areas in Taiwan. In the ZRW, rice, vegetables, and other crops are
88 extensively cultivated. This high agricultural activity underscores the importance of SOC in
89 sustaining soil fertility and agricultural production. In the LRW, SOC plays an essential role in
90 supporting the limited amount of agriculture that is practiced. These two watersheds are located
91 in different climatic zones, which may affect their SOC dynamics. The ZRW is located in
92 central Taiwan and has a subtropical climate, whereas the LRW is located in southern Taiwan
93 and has a tropical monsoon climate. Future climate-change-related changes in temperature and
94 precipitation may substantially affect the content and total stocks of SOC in these two regions,
95 altering their agricultural production and land use patterns.

96   Therefore, this study applied digital soil mapping approaches to generate high-resolution
97 maps of SOC stock distribution in the surface layer (0–30 cm) of the ZRW and LRW in Taiwan,
98 with the aim of better understanding the spatiotemporal dynamics of SOC under different
99 emission scenarios (SSP1-2.6 and SSP2-4.5) and various extreme climate indicators projected
100 for 2050 and 2100.

101

2. Materials and Methods

2.1 Research area

104   The Zhuoshui River watershed (ZRW) is located in central Taiwan. Its basin covers
105 Changhua County, Nantou County, Yunlin County, and Chiayi County. The watershed has an
106 area of 3156.9 km^2 and is located in a subtropical climate zone (Fig. 1a and 1b). This area has
107 an average annual temperature of 8.6–23.6 °C and receives annual cumulative rainfall of
108 834.6–3693.4 mm. The elevation of the study area ranges from 0 to 3844.2 m above sea level,

109 and it has diverse topography consisting of mountains (2060.7 km^2, 65.2%), hills (843.3 km^2,

110 26.6%), and plains (261.7 km^2, 8.2%). In terms of soil classification, the upstream areas are

111 primarily characterized by stony soils, whereas the western plains are predominantly

112 characterized by silty alluvial soils. The Laonong River watershed (LRW) is located in southern

113 Taiwan, representing an upper mainstream area of the Gaoping River. Its basin covers Nantou

114 County, Kaohsiung City, Pingtung County, and Taitung County. The watershed has an area of

115 2038 km^2 and is located in a tropical climate zone. This area has an average annual temperature

116 of 19.5 °C, and it received annual cumulative rainfall of 3222.6 mm during the period 2011–

117 2020. According to the 2015 Land Cover Survey, the upper reaches of the basin are

118 predominantly mountainous areas (73.3%), whereas the downstream gentle slopes and plains

119 are predominantly agricultural areas (10.6%; Fig. S1).

120

2.2 Soil samples and analyses

122 Soil survey data for the period 2012–2020 were obtained from the Taiwan Agricultural

123 Research Institute. A total of 901 topsoil samples (0–30 cm, based on IPCC (2006, 2019a)

124 recommendation) were obtained. Each sample's location was recorded using a handheld global

125 positioning system device. After the samples had been air-dried at room temperature, they were

126 sieved through a 35-mesh screen (0.5 mm sieve opening) and stored in plastic containers. They

127 were then analyzed using the loss-on-ignition (LOI) method (Nelson and Sommers, 1996).

128 Because the LOI method typically overestimates SOC (Li et al., 2021), a correction function

129 was applied to adjust SOC content from LOI values to those obtained using a total organic

130 carbon (TOC) analyzer (solid TOC cube, Elementar). The correction equation is as follows:

131

132 $\qquad$ TOC $= 0.7084 * \text{LOI} - 0.0986$ (R^2 $= 0.94$; P < 0.001) $\qquad$ [1]

133

134 where TOC and LOI refer to the SOC contents (%) determined by the TOC analyzer and

135 the LOI method, respectively. A sample's total bulk density was determined using the clod

136 method or soil core method (Blake and Hartge 1986). Finally, the soil organic carbon stock

137 (SOC$_{stock}$, kg m^{-2}) was calculated using the following equation:

138

$$\text{SOC}_{stock} = \text{TOC} * \rho * D/10 \qquad [2]$$

139

140 where TOC is the SOC content (%), ρ is the bulk density of soil (g cm^{-3}), and D is the soil

depth (cm). Owing to the substantial variability in coarse fragment content, this study excluded them from the calculation of SOC stocks.

2.3 Environmental covariates

Environmental covariates were categorized on the basis of factors pertaining to soil formation, including topographical data such as digital elevation models (DEM), satellite remote sensing imagery, meteorological data, land use survey data, and soil order (Table 1). All environmental covariates were resampled at a spatial resolution of 20 m by using R software version 4.0.5 (R Foundation for Statistical Computing, Vienna, Austria).

The DEM was derived from a 20-m grid numerical terrain model established by the Taiwanese Ministry of the Interior. To create an elevation map, the "Fill Sinks" function of SagaGIS 8.0.1 was used to smooth the discontinuities in the model. These elevation data were employed to generate relevant topographical attributes. These attributes included the slope, aspect, terrain ruggedness index (TRI), terrain position index (TPI), topographic wetness index (TWI), multiresolution index of valley bottom flatness (MrVBF), multiresolution ridge top flatness (MrRTF), curvature, flow accumulation, and stream power index (SPI). Ma et al. (2017) argued that topographical parameters can serve as environmental covariates in organic carbon prediction models.

The normalized difference vegetation index (NDVI) was calculated using infrared (b4) and near-infrared (b8) satellite imagery data (Sentinel 2) for the period 2016–2020 to determine the proportion of space covered by vegetation, which was produced by the Google Earth Engine at a resolution of 20 m. Climate is one of the key soil-forming factors and, according to Wiesmeier et al. (2019), a major driver influencing SOC storage. This study used climatic data from 2011 to 2020, including mean annual temperature (MAT) and total annual precipitation (TAP), obtained from Taiwan's Central Weather Bureau. The original spatial resolution of these data was 1 km. To match the spatial scale of other covariates, these raster layers were resampled to 20 m resolution using the resample function from the raster package in R (Hijmans, 2022), with bilinear interpolation (method = "bilinear"). In addition to these factors, land cover type also influences SOC storage (Edmondson et al., 2014). Therefore, this study used a 2015 land cover map produced by TARI, classified into five categories: (1) paddy fields; (2) upland farming (including miscellaneous grains, tea trees, betel nuts, and bamboo); (3) orchards; (4) forests (including plantations, primary forests, and high-mountain arrow bamboo forests); and (5) others (miscellaneous and riverine lands). The flow chart of the methodology is illustrated

174   in Fig. S2.

175

176   *2.4 Predictive models*

177    Because of research advancements in the field, the techniques used in DSM have evolved

178   from simple linear models to comprehensive machine learning technologies (Minasny and

179   McBratney, 2016). In this study, two widely used data mining models, namely Cubist and RF

180   models, were employed. Both models were further combined with regression kriging to

181   account for both geographical and non-geographical effects, resulting in the Regression

182   Kriging with Cubist and Regression Kriging with Random Forest models. Their capabilities in

183   predicting the spatial distribution of SOC were compared.

184    The Cubist model is a rule-based classification algorithm proposed by Quinlan (1992). It

185   was developed on the basis of the M5 tree model. The Cubist model segregates data into several

186   subsets on the basis of "if–then" patterns and identifies linear relationships between the target

187   variables and environmental covariates in each subset. In the present study, we used the "Cubist"

188   package in R software version 4.0.5 for model development (Kuhn and Quinlan, 2022). We

189   adopted the following parameters: (1) rules for data classification based on rule count, (2)

190   extrapolation for determining the model's degree of extrapolation, and (3) committees that

191   generate multiple committee models on the basis of the number of samples to be processed in

192   the model (i.e., the amount of data) to refine the previous prediction and output collective

193   results. We used the "caret" package (Kuhn, 2008) to perform hyperparameter tuning for the

194   Cubist model, testing committee values of 1, 5, 10, 15, 20, and 25. Using 5-fold cross-

195   validation, caret automatically evaluated the performance of each hyperparameter setting based

196   on the root mean square error (RMSE). The tuning results indicated that setting committees =

197   20 produced the lowest cross-validation RMSE, suggesting that this configuration achieved the

198   highest predictive accuracy. Therefore, committees = 20 was selected as the final model

199   parameter.

200    The RF model is an ensemble learning algorithm introduced by Breiman (2001). This

201   model reconstructs a data set into multiple new sets with identical sample size through random

202   resampling during model training. For each data set, environmental covariates are randomly

203   selected for constructing classification or regression trees. In the case of continuous variables,

204   the model's predicted value is the average output of all regression trees. In this study, we used

205   the "randomForest" package of R software version 4.0.5 for model development (Liaw and

206   Wiener, 2002). We adopted the following parameters: (1) mtry, which determines the number

207 of environmental covariates extracted for each new data set in regression tree construction, and
208 (2) ntree, which determines the number of regression trees in the RF. We used the "caret"
209 package to perform hyperparameter tuning for the Random Forest model. The parameter *mtry*
210 was tested with values ranging from 2 to 9. Using 5-fold cross-validation, *caret* automatically
211 evaluated the performance of each hyperparameter setting based on the root mean square error
212 (RMSE). The tuning results indicated that the model achieved the lowest cross-validation
213 RMSE when *mtry* = 7. The number of trees (*ntree*) was kept at the default value of 500, which
214 is generally sufficient to ensure model stability (Peng et al., 2025). Therefore, the final Random
215 Forest model was trained using *mtry* = 7 and *ntree* = 500.

216

217 ### 2.5 Model training and validation

218 Before model development, we employed the "rpart" package in R software version 4.0.5
219 (Therneau and Atkinson, 2022) to extract 70% of the data as the training data set (calibration
220 set), totaling 600 samples. We used the remaining 301 samples (30%) as the validation data set
221 (validation set) and used it to determine the model's predictive performance. Model
222 performance was evaluated by comparing the predicted values with the observed values in the
223 validation group. Root mean square error (RMSE) and coefficient of determination (R^2) values
224 were used as assessment indicators and calculated as follows:

225

$$RMSE = \sqrt{\frac{1}{n}\sum_{i=1}^{n}(o_i - p_i)^2}, \qquad [3]$$

$$R^2 = \frac{\sum_{i=1}^{n}(p_i - \mu_o)^2}{\sum_{i=1}^{n}(o_i - \mu_o)^2}, \qquad [4]$$

226

227 where p_i and o_i represent the predicted and observed values, respectively, and μ_o represents the
228 mean observed value. Because of the spatial variability of soil properties, effectively
229 quantifying uncertainty in predictive map outputs is crucial. Therefore, in this study, the
230 prediction interval was calculated using 90% quantiles of upper and lower limits of prediction
231 through the bootstrap method (Malone et al., 2014).

232

233 ### 2.6 Geographic information and data analyses

234 In this study, maps were created and spatial statistical analyses were conducted using the
235 geographic information system (GIS) software ArcMap 10.8. Data processing and statistical
236 analyses were conducted using Microsoft Excel 2016 (Microsoft, Redmond, WA, USA) and R

237   software version 4.0.5.

238   Redundancy analysis is a multivariate or multiresponse technique similar to regression. In

239   this study, redundancy analysis was conducted to determine whether extreme climatic indices

240   and SOC stock changes were associated with the matched grid cells (different land types)

241   evaluated in our previous study (Jien et al., 2025). All statistical analyses, unless indicated

242   otherwise, were conducted using SPSS version 18.0 (SPSS, Chicago, IL, USA). A p-value of

243   <0.05 was considered statistically significant. Partial least squares path modeling (PLS-PM)

244   was employed to identify the pathways underlying the study variables, including emission

245   scenarios, extreme climate indices, and SOC stock and land types. A PLS-PM model was

246   constructed using the "innerplot" function of the "plspm" package (Sanchez et al., 2017). The

247   model's quality and performance were evaluated using the goodness-of-fit (GOF) test. Finally,

248   the "ggplot2" package in R software (Wickham, 2016) was used for redundancy analysis and

249   plot generation (Villanueva and Chen, 2019).

250

251   *2.7 Climate data in various emission scenarios and with extreme climate indices*

252   Future climate predictors were obtained from CMIP6-based global climate models,

253   including shared socioeconomic pathways (SSPs) established by the Intergovernmental Panel

254   on Climate Change (IPCC). Model MIROC6—developed by the Japan Agency for Marine-

255   Earth Science and Technology, Atmosphere and Ocean Research Institute, University of

256   Tokyo—was selected for predicting SOC stocks from future climate data. The historical and

257   projected extreme climate indices of CMIP6 were employed for different socioeconomic

258   pathways, specifically for scenarios SSP1-2.6 (sustainable development) and SSP2-4.5 (middle

259   of the road). These data were used to examine climate patterns and trends and establish models

260   for predicting the impact of future climate change on various environments.

261   In this study, we identified the following six extreme climatic indices: consecutive dry

262   days (CDD), consecutive wet days (CWD), very wet day precipitation (R95P), extremely wet

263   day precipitation (R99P), minimum value of daily maximum temperature (TNx), and

264   maximum value of daily maximum temperature (TXx). These indicators provided valuable

265   insights into the effects of extreme weather events across the study area. According to

266   Chalchissa and Kuris (2024), the correlation between these indicators and soil health factors

267   may offer a comprehensive understanding of soil health and the potential for carbon

268   sequestration in agricultural systems.

269

3. Results

3.1 Statistical description of SOC stock

The sampling sites of this study are presented in Fig. S1(a). The average topsoil SOC stock across all sampling points was 4.36 kg m^{-2}. In the ZRW, the topsoil SOC stock ranged from 0.19 to 31.8 kg m^{-2}, with an average of 4.51 kg m^{-2}. In the LRW, the topsoil SOC stock ranged from 0.41 to 14.4 kg m^{-2}, with an average of 3.80 kg m^{-2}. Although the data for the LRW were more concentrated, the overall data exhibited positive skewness, with a skewness value of 0.15. Therefore, a natural logarithm transformation was applied to improve model performance by approximating a normal distribution.

3.2 Model performance in SOC stock prediction

This study constructed SOC stock predictive models using the Cubist, RF, and regression kriging with the training data set and environmental covariates. The performance of these models was evaluated using R^2 and RMSE values. Among the evaluated models, the RF model demonstrated the highest predictive performance in the training data set. The distribution of the training data set (calibration set) and validation data set is depicted in Fig. 2. Therefore, we focused on model performance in the prediction of validation data set prior to model selection. In this respect, the performance indicators of the Cubist model were $R^2 = 0.43$ and RMSE = 0.45 kg m^{-2}, while those of the RF model were $R^2 = 0.46$ and RMSE = 0.43. After incorporating regression kriging, the indicators improved to $R^2 = 0.48$ and RMSE = 0.50 for the Cubist model, and remained at $R^2 = 0.46$ and RMSE = 0.43 for the RF model (Fig. 2).

3.3 Importance analysis of environmental covariate

For the variable importance analysis in the RF model, the increase in mean squared error (MSE) was calculated when each covariate was excluded during the random selection process. In the Cubist model, the usage ratios of various environmental covariates were computed. These indicators revealed the key role of environmental covariates in the prediction of SOC stocks (Fig. 3a). In the RF model, covariates that led to an increase in mean squared error (IncMSE) greater than 15% included elevation (23%), soil order (20%), annual mean temperature (19%), and precipitation (15%). In the Cubist model, the primary classification factors were annual mean temperature (45%), soil order (18%), and elevation (17%). The results of the Cubist model indicated that the importance of aspect, curvature, and flow accumulation was relatively low, thus they exhibited either no usage or very low usage

frequency (Fig. 3a). Among the covariates included, more than half of the data incorporated covariates such as elevation (98%), annual mean temperature (62%), NDVI (59%), TRI (54%), K-value (53%), and slope (52%). These results indicated that climatic and topographic factors strongly contributed to model performances. In summary, the RF and Cubist models identified soil order, elevation, and annual mean temperature as the factors representing the influence of soil, topography, and climate, respectively, on the SOC stock in the study areas.

3.4 Predicted map of SOC stock

The predicted spatial distribution of SOC stock is presented in Fig. 3b. According to the statistical analysis of the prediction map, the mean SOC stock in the ZRW and LRW was 5.51 and 6.38 kg m^{-2}, respectively. The first quartile, median, and third quartile were 3.85, 5.31, and 6.88 kg m^{-2}, respectively, for the ZRW and 3.80, 5.96, and 8.85 kg m^{-2}, respectively, for the LRW. A reduction in SOC stock from mountainous areas to lowland areas (plain areas) was found for both watersheds. In addition, high SOC stock (approximately 15 kg m^{-2}) was discovered in southeastern areas in the ZRW and in northeastern areas in the LRW. Lower storage values of <3 kg m^{-2} were found in downstream areas in the LRW and near the estuary in the ZRW. The areas located along the downstream plains of ZRW exhibited low SOC stock (<2.5 kg m^{-2}) near the river, with SOC stock higher farther from the river.

3.5 Uncertainty analysis for predictive models

For each sampling point in the training data set, prediction residuals were established through leave-one-out cross-validation for the regression kriging and Cubist models. The study area was then classified by landscape in accordance with the classification rules of the Cubist model (Table 2). Fig. 4 presents 90% confidence interval maps drawn using data segmentation and cross-validation techniques. These prediction limit intervals can be regarded as indicators of the model's uncertainty. In the downstream areas of the study region, the confidence interval widths were generally below 6 kg m^{-2}, whereas in the mountainous regions they were substantially higher, with some areas reaching up to 40 kg m^{-2}.

3.6 SOC stock distribution with various landscape types and land uses

The SOC stock spatial distribution was categorized on the basis of topography to demonstrate the distribution of SOC stocks under various landscape types. As shown in Fig. 5, in the lowlands of the ZRW, the lowest average SOC stock was identified in upland farming

336 areas (1.93 kg m^{-2}), whereas the highest average SOC stock was identified in paddy fields (3.08

337 kg m^{-2}). In the lowlands of the LRW, the lowest average SOC stock was identified in "other"

338 land cover types (1.89 kg m^{-2}), whereas the highest average SOC stock was identified in forest

339 areas (3.17 kg m^{-2}). In the uplands of both catchments, the lowest cover was identified in paddy

340 fields (3.01 and 2.16 kg m^{-2}), whereas the highest cover was identified in forests (4.22 and 3.6

341 kg m^{-2}). In terms of land cover, the highest SOC stock was identified in forest areas, with 6.54

342 kg m^{-2} in the ZRW and 8.02 kg m^{-2} in the LRW, whereas the lowest SOC stock was identified

343 in orchard areas, with 4.82 kg m^{-2} in the ZRW and 5.60 kg m^{-2} in the LRW.

344

345 ### *3.7 Extreme climate index parameter estimates in two emission scenarios*

346 Extreme climate indices in two SSPs were compared: SSP1-2.6 (sustainable development)

347 and SSP2-4.5 (middle of the road). Projections were evaluated for mid-century (2050) and end-

348 century (2100) time points at units of sub-catchment for each watershed. These units were

349 classified as total area, lowlands, uplands, and mountainous areas, denoted as T, L, U, and M,

350 respectively, in Tables S1 and S2.

351 In all emission scenarios, major spatial heterogeneity and temporal increases were found

352 in SOC stocks (Table 3, Figs. 6 and 7). These findings underscore the importance of modifying

353 the management practices of land use in the future, especially if climate change is severe. In

354 mountainous areas in both watersheds, significant SOC accumulation was predicted. By

355 contrast, lowland agricultural zones are expected to maintain relatively low SOC stocks (<9

356 Mg C ha^{-1}), with minor gains across scenarios. Scenario SSP2-4.5 was found to result in the

357 higher projected increase in SOC stocks as a result of elevated CO_2 and potential biomass input,

358 although spatial disparities are expected to increase, particularly in erosion-prone or intensively

359 cultivated lands (Fig. S3).

360 The CDD, CWD, R95p/R99p, and TNx/TXx were analyzed as extreme climate indices. In

361 both SSPs, the increases in temperature- and precipitation-related extremes in the two

362 watersheds were significant. In scenario SSP2-4.5, the magnitude and spatial heterogeneity of

363 these changes were predicted to intensify toward 2100 compared to the 2020 baseline (Fig. 6a).

364 In the ZRW, scenario SSP2-4.5 was predicted to result in a 36% increase in CDD, especially

365 by 2050 in mountainous areas (Table S1). For scenario SSP1-2.6, the CDD was predicted to

366 decrease slightly by 26.3% and 35.2%, particularly in lowlands and uplands. For both

367 watersheds, CWD was predicted to increase in the emission scenarios for 2050 and 2100, but

368 different trends were discovered for the ZRW and LRW. Regarding the ZRW, CWD was

predicted to significantly increase in lowlands and decrease in mountainous areas. However, in the LRW, it was predicted to increase only in uplands (Fig. 6a). These results indicated the polarization of wet–dry periods. A major increase in rainfall extremes was predicted, with R95p increasing by 1785 mm and 1889 mm in the total and mountainous areas, respectively, under the scenario SSP2-4.5 by 2100 in the ZRW. For the same scenario and time frame, R99p was predicted to reach 3535 mm in total areas, with uplands and mountainous areas receiving rainfall of 3625 and 3588 mm, respectively. Temperature extremes were also predicted to increase, where the TXx in ZRW was predicted to increase by up to 22.7% in mountainous areas (scenario SSP1-2.6 and SSP2-4.5 for the year 2100), whereas TNx was predicted to increase by 53.7% in mountainous areas under the scenario SSP2-4.5 by 2100, indicating pronounced warming.

Regarding the LRW, which is characterized by a tropical monsoon climate, high warming and precipitation extremes were predicted, particularly in uplands and mountainous areas, indicating climate spatial heterogeneity. For scenario SSP1-2.6, an approximately 22.2% CDD increase for the entire watershed was predicted by 2100 (Table S2), with the largest increase predicted for lowland areas (52.9%). In the mountainous areas, R95p and R99p under scenario SSP2-4.5 were predicted to reach 1142 mm and 3525 mm, respectively, by 2100. Moreover, CWD was predicted to increase in uplands by up to 85.7%, suggesting prolonged wet conditions. Notably, under the same scenario and time, TXx and TNx were predicted to substantially increase in uplands and mountainous areas, reaching up to 26.8% and 62.6%, respectively, emphasizing the intensification of heat extremes. Overall, this scenario may present another type of threat: long-term droughts with torrential downpours and extreme heat.

3.8 Relationships between extreme climate indices and SOC stocks

Principal component analysis (PCA) was conducted to examine the relationships between extreme climate indicators and SOC stock and to determine their topographic distribution characteristics for two scenarios. Regarding scenario SSP1-2.6, SOC stock variation exhibited negative correlations with R95p and R99p, indicating that extreme precipitation may be detrimental to the maintenance of SOC stocks (Fig. 8a). Pearson's correlation analysis revealed significant negative correlations of SOC stocks with R95p ($r = -0.32$, $p < 0.05$) and R99p ($r = -0.29$, $p < 0.01$; Fig. 8b). Regarding scenario SSP2-4.5, SOC stock variation exhibited a positive correlation with R95p and R99p with $r = 0.17$ and $r = 0.18$, ($p < 0.05$), respectively (Fig. 8c and 8d), indicating that stable wet conditions may promote

SOC accumulation under moderate emission conditions. For all scenarios, strong positive R95p–R99p and TXx–TNx correlations were found (e.g., $r = 0.93$ between R95p and R99p in scenario SSP2-4.5). Taken together, these findings suggest uniform increases in the frequencies of extreme rainfall and extreme heat events in terms of both spatial distribution and climatic mechanisms.

Our results revealed clear topographic effects, with distinct spatial variations in SOC stock dynamics predicted for the different emission scenarios. For scenario SSP1-2.6, SOC stocks were projected to decrease by 3% to 21%, whereas for scenarios SSP2-4.5, SOC stocks were projected to increase by 7.91% to 58.3%, particularly in mountainous areas (because of their enhanced net primary productivity). In addition, the variance and coefficient of variation (CV) of SOC stock percentages show a significant increase in interquartile range and CV over time under SSP1-2.6 and SSP2-4.5 emission scenarios relative to the 2020 baseline. For both emission scenarios, the variance and coefficient of variation of the SOC stock percentage distribution were predicted to increase (Table 3). Collectively, these results indicate that future climatic extremes are projected to significantly increase the spatial heterogeneity of the percentage distribution of SOC stocks. In the majority of scenarios, uplands and mountainous areas are expected to exhibit a drastic response to extreme climate indicators, including major increases in CDD, R99p, TXx, and TNx. In uplands, SOC stocks are expected to respond strongly to the extreme climate, suggesting the susceptibility of slope soils to extreme rainfall and thermal destabilization. Furthermore, more extreme values are predicted for the LRW than for the ZRW, which is likely attributable to the topographic elevation distribution and baseline tropical monsoon climate in the LRW.

In our PLS-PM analysis, we discovered a goodness of fit (GOF) value ranging from 43.0 to 45.7, indicating the high explanatory power of our findings (Fig. 9). The PLS-PM results also revealed distinct differences in the controls for SOC stocks between the ZRW and LRW. For the ZRW (GOF = 45.7%), topographic variables (elevation and slope gradient) were found to have the strongest positive total effect on SOC stocks (standardized total effect = 0.579), followed by consecutive dry and wet periods (CDD and CWD, total effect = 0.238). Despite these findings, extreme rainfall events and temperature did not appear to have a direct effect on SOC stocks. For the LRW (GOF = 43.0%), stronger topographic control of SOC stocks was discovered (total effect = 0.753), with the direct path being positive (0.84, $p < 0.01$), indicating that the SOC accumulation patterns observed predicted this watershed will be closely linked to its land type. Regarding scenarios SSP2-4.5, most of the predicted increases in SOC stocks are

concentrated in mountainous areas. Despite these results, the effects of temperature extremes on SOC stocks will presumably be weakened by topographic and hydrological stability, particularly in the LRW. For both watersheds, prolonged dry spells were predicted to indirectly increase SOC stocks, whereas rainfall extremes were predicted to reduce SOC stocks, particularly in uplands (slope lands). Taken together, these findings underscore the importance of incorporating topographic and extreme climate variables into SOC modeling and climate-resilient soil management strategies.

4. Discussion

4.1 Ability of machine learning models to predict SOC stocks

Lamichhane et al. (2019) argued that several predictive models can be used to predict the spatial distribution of SOC. In the present study, common machine learning models—the Cubist, RF, and regression kriging models—were used to predict SOC stock in the sampling area. Shaik and Srinivasan (2019) highlighted the likelihood of overfitting in RF models, indicating that while the model may predict training data accurately, it may perform poorly when applied to unseen data outside the training set. Therefore, in this study, some of the collected data were randomly selected for validation (Fig. 2). The results indicated that integrating regression kriging into the Cubist model yielded the highest predictive performance ($R^2 = 0.48$, RMSE = 0.50), which was significantly higher than that achieved by the Cubist model alone ($R^2 = 0.43$, RMSE = 0.45). However, incorporation of regression kriging into the RF model resulted in limited improvements, consistent with the results of Vaysse and Lagacherie (2015). This limited improvement may be attributable to the inherently low residuals in the RF model, indicating that even standardizing these residuals and adding them to the model would have minimal effects on predictions. As shown in Fig. 4, SOC stocks were underestimated for several samples from mountainous regions with high organic carbon stock due to plant residues, suggesting that this type of variance was not captured by the models or residuals. Other studies have demonstrated various predictive disparities. These studies include those conducted by Lacoste et al. (2014), who applied a Cubist model to predict organic carbon stock in a France-based study ($R^2 = 0.12$, RMSE = 12.64); Adhikari et al. (2014), who employed regression kriging in a Denmark-based study ($R^2 = 0.41$, RMSE = 0.24); and Ma et al. (2017), who combined regression kriging with a Cubist model in a China-based study ($R^2 = 0.25$, RMSE = 0.12). Although the models used in the present study exhibited several predictive disparities, they nonetheless exhibited high reliability in terms of their overall predictive ability.

468   In SOC stock forecasting models, empirical estimations of uncertainty involve geographic
469   spatial segmentation. In Cubist models, input data are divided into groups on the basis of a
470   series of rule-based classifications. Therefore, examining the empirical distribution of the
471   regression kriging residuals in each category is appropriate (Malone et al., 2014). According to
472   classification rules, if low-elevation areas such as plains, foothills, and valleys involve young,
473   weakly developed soils or miscellaneous lands, these areas are considered to exhibit a wide
474   distribution of residuals. By contrast, other soil order categories are considered to exhibit a
475   more concentrated distribution of residuals. In mountainous regions, classification is based on
476   the NDVI, where a higher NDVI indicates more vegetation, whereas a low NDVI suggests the
477   presence of water bodies or bare soils. In this study, analysis of 90% confidence interval maps
478   (Fig. 4) revealed that for low-altitude areas with high sampling density, abundant data were
479   available for model construction, leading to generally low prediction residuals. Even with
480   various landscape classifications, the prediction limit intervals were low. By contrast, in
481   mountainous areas, the existence of few samples and substantial variability in environmental
482   covariates increased the difficulty of prediction. Generally, when establishing empirical
483   divisions with insufficient data, outliers can easily influence the residual distribution in a given
484   category. Therefore, future sample planning in these areas can be guided by such map data.
485

486   *4.2 Effects of environmental covariates on SOC stocks*

487   In this study, SOC stocks were influenced by the following key topographical attributes:
488   elevation, the multiresolution index of valley bottom flatness, slope, and the topographic
489   wetness index (Fig. 3a). As reported by Mishra and Riley (2015), who conducted an Alaska-
490   based study, elevation is a crucial predictor of SOC stock, regardless of resolutions. According
491   to Adhikari et al. (2014), the multiresolution index of valley bottom flatness (MrVBF) and the
492   topographic wetness index (TWI) are important covariates, ranking just below precipitation.
493   The MrVBF is used to identify flat valley bottoms and thereby indicate potential areas of
494   erosion or deposition, whereas the TWI is used to indicate terrain's control over soil moisture,
495   reflecting wet or dry conditions (Lamichhane et al., 2019). Slope affects SOC stocks by
496   influencing solar radiation and moisture retention. Regarding meteorological covariates,
497   annual cumulative precipitation and mean annual temperature are crucial in determining SOC
498   stock. Gray et al. (2015) identified positive correlations of the SOC content of topsoil in New
499   South Wales, Australia, with precipitation and relative humidity. According to Lamichhane et
500   al. (2019), high precipitation may enhance vegetation growth or create anoxic conditions that

slow soil carbon oxidation. Rial et al. (2017) reported a negative correlation between temperature and SOC content in Europe, with higher altitude and latitude found to correspond to slower SOC decomposition. In the present study, the effect of elevation was attributable to temperature, particularly because the original resolution of the temperature data was 1 km, and high-resolution elevation data were necessary to obtain a detailed spatial distribution. Of the two biotic factors used in this study, the NDVI was the primary environmental covariate. Wang et al. (2018) highlighted the role of the NDVI as an indicator of vegetation cover, which is strongly correlated with SOC. They emphasized that convincing results could be obtained if long-term remote sensing data could be obtained to calculate NDVI values for multiple time periods.

4.3 Influence of land cover on the spatial distribution of SOC stocks

In this study, a trend of increasing SOC stock with increasing elevation was discovered, and this effect is likely driven by elevation and temperature (Fig. 3b, Fig. S3). The SOC stock in differing land coverage types was found to exhibit variation for different terrains. For instance, for lowlands, SOC stocks are predicted to rapidly decrease as a result of intensive cultivation, leading to low SOC stocks in agricultural production lands (Fig. 3b). Regarding the LRW, which has a tropical climate, SOC stock in farmlands was considerably lower than that in forests. This finding may be attributable to the farmlands in the LRW being frequently tilled for triple cropping or the mean annual temperature in the area being higher than that on the Zhuoshui River plains. In uplands, the rice fields in the two basins had SOC stock levels similar to those observed for lowlands, although an increase was discovered for orchard and forests. In mountainous areas, the SOC stock predictions were higher than those for lowlands and uplands across all types of land cover. According to the literature, the eastern region of the LRW experiences high precipitation and low temperatures, which result in higher organic carbon storage than that observed in the ZRW, particularly in mountainous areas (Fig. 3b; Guo et al., 2019). Furthermore, forests cover the majority of the landscape in mountainous areas and represent the primary reservoirs of SOC stocks.

4.4. Adaptation strategies for the management of SOC stocks in various emission scenarios

In this study, future climatic variables calculated from global climate models (GCMs) were used as inputs to estimate the spatiotemporal variation in global topsoil organic carbon stocks in 2020, 2050, and 2100. All GCM were obtained from the Coupled Model Intercomparison

Project. CMIP6 was specifically selected for estimating future topsoil organic carbon stocks. Tables S1 and S2 list the extreme climate indicators involved in the considered scenarios (scenarios SSP1-2.6 and SSP2-4.5) on the basis of CMIP6 data.

Our results indicated increasingly pronounced spatial heterogeneity in SOC stocks in the scenario involving severe greenhouse gas emissions (Table 3, Fig. 6). Severe warming in the future will cause increasingly regional climate variability, resulting in greater spatial heterogeneity in SOC stocks. This phenomenon will be particularly evident in countries with complex topography, such as those located on the frontline of the Pacific Rim, which is directly exposed to the threats of rapid climate change. Generally, the combination of steep terrain and intricate terrain complicates management of the SOC distribution because spatial variability driven by extreme climatic events is difficult to predict and control.

According to our results, extreme climate and land type are the most crucial determinants of SOC stocks in regions near the Pacific Rim (Dialynas et al., 2016; Wei et al., 2024; Chen et al., 2024). As shown in Figs. 6 and 7c, in scenario SSP1-2.6, SOC stocks are projected to be depleted by 2050 (−21%) and 2100 (−3.75%), with this depletion most severe in lowlands and uplands (slope lands). A significant increase in R95p, R99p, or CWD may increase soil erosion, leading to major losses in SOC stocks. Intense rainfall events may also cause topsoil erosion and the leaching of dissolved organic carbon, and episodic carbon export may exceed respiratory losses (Olaya-Abril et al., 2017; Rillig et al., 2021). In certain mountainous areas, localized SOC gains are predicted, even for the low emission projections, which may be related to spatially uneven warming and rainfall, leading to enhanced vegetation productivity and underground carbon input (Fig. 6; Guo et al., 2019). These findings are consistent with the region-specific SOC responses to temperature and precipitation anomalies in previous modeling studies (Wang et al., 2023).

In scenario SSP2-4.5, which involves CO_2 emissions that approach the current levels until the mid-century time point before declining but do not reach net zero by 2100, the SOC stocks are predicted to be controlled by R95p, R99p, and TXx (not statistically significant). For all study areas, slight warming and increased extreme rainfall events (smallest increase among all emission scenarios) will facilitate vegetation growth, which will in turn increase SOC stocks. Despite these findings, losses in SOC stocks are still predicted to occur in certain upland regions (Fig. 6) as a result of erosion events caused by increases in CWD, particularly in the LRW. Overall, these results underscore the importance of drainage devices and specific agricultural management practices in uplands (Vereecken et al., 2022; Wang et al., 2023).

In contrast to previous findings, our results indicate that SOC stocks will likely increase by an average of 14.2% to 35.5% in the total study area under scenario SSP2-4.5 (Fig. 7c). Under this scenario, TNx and TXx are crucial factors influencing SOC stocks, particularly due to increased net primary productivity driven by warming temperatures, CO_2 fertilization, and extended growing seasons that promote vegetation growth. (Elbasiouny et al., 2022). When the amount of biomass, including wood debris and roots, increases, more biomass can be transformed into stable SOC for storage. This finding is consistent with the microbial efficiency matrix stabilization framework, which treats root-derived microbial residues as the main precursors to mineral-associated organic matter, a stable SOC pool (Cotrufo et al., 2013; Sokol and Bradford, 2019).

Based on the SSP1-2.6 and SSP2-4.5 emission scenarios, severe warming and prolonged droughts in mountainous areas may result in wildfires or drought-induced dieback, which may reverse previous carbon gains in cases of ecological equilibrium within forests. These climate conditions may overwhelm current agricultural systems and infrastructure and undermine the current ecological carrying capacity (Zhang et al., 2020). Although a slight increase in SOC stocks was projected on the emission scenarios, some uplands will experience clear losses in SOC stocks. Previous study reported a reduced SOC stocks in slope-lands (Sarstedt et al., 2014). This effect indicates the vulnerability of uplands to erosion caused by runoff under extreme precipitation, thereby threatening long-term carbon retention. As observed in this study, the increases in CDD might decrease vegetation growth and soil moisture, which in turn will lead to less organic input and greater carbon losses. This condition is common in uplands, not mountainous areas, because the effects of temperature extremes on SOC stocks may be weakened by topography. These findings were confirmed by our PLS-PM analysis (Fig. 9). In terms of strategies for adaptation to temperature extremes, firebreak corridors or buffer zones in mountainous areas and drainage constructions in uplands should be prioritized.

Although the Cubist, Random Forest, and regression kriging models in this study demonstrated reasonable predictive performance, several limitations should be acknowledged. First, these models are data-driven and have limited extrapolation ability in regions beyond the range of the training data (Meyer and Pebesma, 2021). In addition, the uneven distribution of soil samples represents a major source of uncertainty; the scarcity of sampling points in mountainous areas results in higher prediction uncertainty (Jien et al., 2025). These limitations should be considered when interpreting the model results and the spatial distribution of SOC. In addition to climatic factors, land type plays a major role in SOC stock responses. In this

study, mountainous areas were found to have higher levels of SOC and to be more sensitive to climate change compared with other land types. The varied responses across different land types emphasize the need to include topography, climate, and land management practices in SOC stock models and the importance of developing carbon mitigation strategies (IPCC, 2019b). Ultimately, these findings highlight the importance of topography, climate, and land type as essential factors for improving SOC predictions and guiding carbon management planning.

5. Conclusions

This study established effective DSM models for predicting SOC stock, achieving an R^2 range of 0.43–0.50, and identified key environmental covariates, such as topography, climate, NDVI, and the prediction interval maps for identifying areas not covered in the sampling distribution. The findings suggest that even with observed predictive disparities, the Regression Kinging with Cubist and RF models can still be relied upon for overall predictive ability. The results demonstrated spatio-temporal variability in projected topsoil SOC under different emission scenarios, with clear sensitivity to landscape type and climate extremes. Under a moderate emissions scenario, SOC dynamics were highly sensitive to extreme climate events, with land type also playing a key role. These effects pose both location- and time-specific challenges for SOC management in studies on mid- to late-century time points. In the low-emission scenario (scenario SSP1-2.6), extreme rainfall events are predicted to induce a significant reduction in SOC stocks through erosion in upland areas. However, in the moderate emission scenarios (scenario SSP2-4.5), warming (TNx and TXx) and extreme rainfall events (R95p and R99p) may simultaneously increase biomass input and increase soil erosion risks.

These findings indicate that SOC management strategies should be highly specific to the site and time. In mountainous areas of the ZRW and LRW, even though the SOC stock dynamics in mountainous areas are likely to be affected by extreme rainfall events, heat waves, and prolonged droughts, future mitigation strategies should focus on reducing warming, preventing wildfires, and promoting heat-tolerant tree species. In upland areas, SOC stock changes in ZRW and LRW are predicted to be mainly driven by R95p, R99p, and CWD, where significant SOC losses will occur in certain upland areas for all emission scenarios. Therefore, management strategies should emphasize soil and water conservation to ensure that excess rainfall can be infiltrated into the soil without triggering erosion. These strategies should include the implementation of eco-engineering techniques on slope lands, maintaining vegetation cover and soil permeability, and establishing effective drainage systems. Overall,

clarifying the interactions between climatic extremes, land types, and SOC stocks to develop site-specific management practices is key to enhancing soil's resilience to sustain ecosystem functions in a changing climate.

Funding

This work was supported by the National Science and Technology Council of Taiwan (NSTC 113-2321-B-005-004 and NSTC 112-2313-B-005-059-MY2).

CRediT authorship contribution statement

SHJ: Writing—Review & Editing, Writing—Original Draft, and Data Curation. **CHS and CCY:** Methodology, Investigation, and Conceptualization. **SM and BJY:** Visualization and Methodology. **YMT:** Writing—Review & Editing.

Declaration of competing interests

The authors confirm that they have no financial or personal relationships that could have appeared to influence the research presented in this paper.

Data availability

The data used or analyzed in this study are available from the corresponding author upon reasonable request.

References

Adhikari, K., Hartemink, A. E., Minasny, B., Bou Kheir, R., Greven, M. B., and Greve, M. H.: Digital mapping of soil organic carbon contents and stocks in Denmark, PLoS ONE 9, e105519, https://doi.org/10.1371/journal.pone.0105519, 2014.

Blake, G. R., and Hartge, K. H.: Bulk density, in: Klute, A. (Ed.), Methods of soil analysis. Part 1. Physical and Mineralogical Methods, 2nd ed. ASA, SSSA, Madison, WI, 363–375, https://doi.org/10.2136/sssabookser5.1.2ed.c13, 1986.

Breiman, L.: Random forests, Machine Learning. 41, 5–32, https://doi.org/10.1023/A:1010933404324, 2001.

Chalchissa, F. B., and Kuris, B. K.: Modeling the impacts of extreme climate scenarios on soil acidity (pH and exchangeable aluminum) in Abbay River Basin, Ethiopia, Heliyon, 10, 12, e33448, https://doi.org/10.1016/j.heliyon.2024.e33448, 2024.

666   Chalchissa, F. B., Diga, G. M., Feyisa, G. L., and Tolossa, A.R.: Impacts of extreme
667   agroclimatic indicators on the performance of coffee *(Coffea arabica L.)* aboveground
668   biomass in Jimma Zone, Ethiopia, Heliyon, 8, 8, e10136,
669   https://doi.org/10.1016/j.heliyon.2022.e10136, 2022.

670   Chen, F., Wang, S. J., Dong, Q. J., Esper, J., Büntgen, U., Meko, D., Linderholm, H. W., Wang,
671   T., Yue, W. P., Zhao, X. E., Hadad, M., González-Reyes, Á., and Chen, F.H.: Role of
672   Pacific Ocean climate in regulating runoff in the source areas of water transfer projects on
673   the Pacific Rim. npj Clim, Atmos. Sci., 7, 153, https://doi.org/10.1038/s41612-024-00706-
674   1, 2024.

675   Cotrufo, M. F., Wallenstein, M. D., Boot, C. M., Denef, K., and Paul, E.: The Microbial
676   Efficiency-Matrix Stabilization (MEMS) framework integrates plant litter decomposition
677   with soil organic matter stabilization: do labile plant inputs form stable soil organic matter?,
678   Glob. Chan. Bio., 19, 988–995, https://doi.org/10.1111/gcb.12113, 2013.

679   Dialynas, Y. G., Bastola, S., Bras, R. L., Billings, S. A., Markewitz, D., and Richter, D. d B.:
680   Topographic variability and the influence of soil erosion on the carbon cycle, Glob.
681   Biogeochem. Cycles, 30, 644–660, https://doi.org/10.1002/2015GB005302, 2016.

682   Edmondson, J. L., Davies, Z. G., McCormack, S. A., Gaston, K. J., and Leake, J.R.: Land–
683   cover effects on soil organic carbon stocks in a European city, Sci. Total Environ, 472,
684   444–453, https://doi.org/10.1016/j.scitotenv.2013.11.025, 2014.

685   Elbasiouny, H., El-Ramady, H., Elbehiry, F., Rajput, V. D., Minkina, T., and Mandzhieva, S.:
686   Plant Nutrition under Climate Change and Soil Carbon Sequestration, Sustainability, 14,
687   914, https://doi.org/10.3390/su14020914, 2022.

688   Grace, J.: Understanding and managing the global carbon cycle, J. Ecol., 92, 189–202,
689   https://doi.org/10.1111/j.0022-0477.2004.00874.x, 2004.

690   Gray, J. M., Bishop, T. F. A., and Wilson, B. R.: Factors controlling soil organic carbon stocks
691   with depth in eastern Australia, Soil Sci. Soc. Am. J., 79, 1741–1751,
692   https://doi.org/10.2136/sssaj2015.06.0224, 2015.

693   Grunwald, S.: Multi–criteria characterization of recent digital soil mapping and modeling
694   approaches, Geoderma, 152, 195–207, https://doi.org/10.1016/j.geoderma.2009.06.003,
695   2009.

696   Guo, L., Shi, T. Z., Linderman, M., Chen, Y. Y., Zhang, H. T., and Fu, P.: Exploring the
697   Influence of Spatial Resolution on the Digital Mapping of Soil Organic Carbon by

Airborne Hyperspectral VNIR Imaging, Remote Sens, 11, 1032, https://doi.org/10.3390/rs11091032, 2019.

Hijmans, R. J. raster: Geographic data analysis and modeling. https://doi.org/10.32614/CRAN.package.raster, 2022.

IPCC: 2006 IPCC Guidelines for National Greenhouse Gas Inventories: Agriculture, Forestry and Other Land Use. Volume 4, https://www.ipcc-nggip.iges.or.jp/public/2006gl/vol4.html (last access: October 22, 2025), 2006.

IPCC: 2019 Refinement to the 2006 IPCC Guidelines for National Greenhouse Gas Inventories: Agriculture, Forestry and Other Land Use. Volume 4, https://www.ipcc-nggip.iges.or.jp/public/2019rf/vol4.html (last access: October 22, 2025), 2019a.

IPCC: Climate Change and Land: Special Report on Climate Change, Desertification, Land Degradation, Sustainable Land Management, Food Security, and Greenhouse Gas Fluxes in Terrestrial Ecosystems, https://doi.org/10.1017/9781009157988, 2019b.

Jenny, H.: Factors of soil formation: a system of quantitative pedology, McGraw Hill, New York, 1941.

Jien, S. H., Minasny, B., Yang, B. J., Liu, Y. T., Yen, C. C., Ocba, M. A., Zhang, Y. T., and Syu, C. H.: Enhancing Soil Carbon Storage: Developing high-resolution maps of topsoil organic carbon sequestration potential in Taiwan, Geoderma, 459, 117369, https://doi.org/10.1016/j.geoderma.2025.117369, 2025.

Johnston, C. A., Groffman, P., Breshears, D. D., Cardon, Z. G., Currie, W., Emanuel, W., Gaudinski, J., Jackson, R. B., Lajtha, K., Nadelhoffer, K., Jr., D. N., and Post, W. M.: Carbon cycling in soil. Front, Ecol. Environ, 2, 522–528, https://doi.org/10.1890/1540-9295(2004)002[0522:CCIS]2.0.CO;2, 2004.

Keskin, H., and Grunwald, S.: Regression kriging as a workhorse in the digital soil mapper's toolbox, Geoderma, 326, 22–41, https://doi.org/10.1016/j.geoderma.2018.04.004, 2018.

Kuhn, M.: Building Predictive Models in R Using the caret Package. Journal of Statistical Software, 28(5), 1–26. https://doi.org/10.18637/jss.v028.i05, 2008.

Lacoste, M., Minasny, B., McBratney, A., Michot, D., Viaud, V., and Walter, C.: High resolution 3D mapping of soil organic carbon in a heterogeneous agricultural landscape, Geoderma, 213, 296–311, https://doi.org/10.1016/j.geoderma.2013.07.002, 2014.

Lamichhane, S., Kumar, L., and Wilson, B.: Digital soil mapping algorithms and covariates for soil organic carbon mapping and their implications: A review, Geoderma, 352, 395–413, https://doi.org/10.1016/j.geoderma.2019.05.031, 2019.

731   Li, H. W., Wu, Y. P., Chen, J., Zhao, F., Wang, F., Sun, Y. H., Zhang, G. C., and Qiu, L. J.:
732   Responses of soil organic carbon to climate change in the Qilian Mountains and its future
733   projection, J. Hydrol, 596, 126110, https://doi.org/10.1016/j.jhydrol.2021.126110, 2021.

734   Liaw, A., and Wiener, M.: Classification and regression by RandomForest, R news, 2, 18-22,
735   https://CRAN.R-project.org/doc/Rnews/, 2002.

736   Ma, Y. X., Minasny, B., and Wu, C.: Mapping key soil properties to support agricultural
737   production in Eastern China, Geoderma Regional, 10, 144–153,
738   https://doi.org/10.1016/j.geodrs.2017.06.002, 2017.

739   Malone, B. P., Minasny, B., POdgers, N., and McBratney, A. B.: Using model averaging to
740   combine soil property rasters from legacy soil maps and from point data, Geoderma, 232,
741   34–44, https://doi.org/10.1016/j.geoderma.2014.04.033, 2014.

742   McBratney, A. B., Santos, M. M., and Minasny, B.: On digital soil mapping, Geoderma, 117,
743   3–52, https://doi.org/10.1016/S0016-7061(03)00223-4, 2003.

744   Meyer, H., & Pebesma, E.: Predicting into unknown space? Estimating the area of applicability
745   of spatial prediction models. Methods in Ecology and Evolution, 12(9), 1620-1633,
746   https://doi.org/10.1111/2041-210X.13650, 2021.

747   Minasny, B., and McBratney, A.B.: Digital soil mapping: A brief history and some lessons,
748   Geoderma, 264, 301–311, https://doi.org/10.1016/j.geoderma.2015.07.017, 2016.

749   Mishra, U., and Riley, W. J.: Scaling impacts on environmental controls and spatial
750   heterogeneity of soil organic carbon stocks, Biogeosciences, 12, 3993–4004,
751   https://doi.org/10.5194/bg-12-3993-2015, 2015.

752   Nelson, D. A., and Sommers, L.E.: Total carbon, organic carbon, and organic matter, in: Sparks,
753   D.L. (Ed.), Methods of soil analysis. Part 3, Chemical Methods. ASA, SSSA, Madison,
754   WI, 961–1010, https://doi.org/10.2136/sssabookser5.3.c34, 1996.

755   Olaya-Abril, A., Parras-Alcántara, L., Lozano-García, B., and Obregón-Romero, R.: Soil
756   organic carbon distribution in Mediterranean areas under a climate change scenario via
757   multiple linear regression analysis, Sci. Total Enviro., 592, 134–143,
758   https://doi.org/10.1016/j.scitotenv.2017.03.021, 2017.

759   Peng, Y., Zhou, W., Xiao, J., Liu, H., Wang, T., & Wang, K.: Comparison of Soil Organic
760   Carbon Prediction Accuracy Under Different Habitat Patches Division Methods on the
761   Tibetan Plateau. Land Degradation & Development. https://doi.org/10.1002/ldr.70184,
762   2025.

763 Quinlan, J.R.: Learning with Continuous Classes, in: Proceedings of Australian Joint
764   Conference on Artificial Intelligence, Hobart, 1992.

765 Rial, M., Cortizas, A. M., and Rodríguez-Lado, L.: Understanding the spatial distribution of
766   factors controlling topsoil organic carbon content in European soils, Sci. Total Enviro.,
767   609, 1411–1422, https://doi.org/10.1016/j.scitotenv.2017.08.012, 2017.

768 Rillig, M. C., Leifheit, E., and Lehmann, J.: Microplastic effects on carbon cycling processes
769   in soils, PLoS Biol., 19, e3001130, https://doi.org/10.1371/journal.pbio.3001130, 2021.

770 Rudiyanto, Minasny, B., Setiawan, B. I., Saptomo, S. K., and McBratney, A. B.: Open digital
771   mapping as a cost-effective method for mapping peat thickness and assessing the carbon
772   stock   of   tropical   peatlands,   Geoderma,   313,   25–40,
773   https://doi.org/10.1016/j.geoderma.2017.10.018, 2018.

774 Sanchez, G., Trinchera, L., Russolillo, G.: plspm: tools for partial least squares path modeling
775   (PLS-PM), R Package Version (4), p. 9 https://CRAN.R-project.org/package=plspm, 2017

776 Sarstedt, M., Ringle, C. M., Smith, D., Reams, R., and Hair, J. F.: Partial least squares structural
777   equation modeling (PLS-SEM): A useful tool for family business researchers, J. Fam. Bus.
778   Strategy, 5, 105–115, https://doi.org/10.1016/j.jfbs.2014.01.002, 2014.

779 Shaik, A. B., and Srinivasan, S.: A Brief Survey on Random Forest Ensembles in Classification
780   Model, in: Bhattacharyya, S., Hassanien, A., Gupta, D., Khanna, A., Pan, I. (Eds.),
781   International Conference on Innovative Computing and Communications. Lecture Notes
782   in Networks and Systems, 56. Springer, Singapore, 253–260, 2019.

783 Siewert, M. B.: High-resolution digital mapping of soil organic carbon in permafrost terrain
784   using machine learning: a case study in a sub-Arctic peatland environment, Biogeosci., 15,
785   1663–1682, https://doi.org/10.5194/bg-15-1663-2018, 2018.

786 Singh, B. P., Setia, R., Wiesmeier, M., and Kunhikrishnan, A.: Chapter 7 - Agricultural
787   management practices and soil organic carbon storage, Soil carbon storage, 207–244,
788   https://doi.org/10.1016/B978-0-12-812766-7.00007-X, 2018.

789 Sokol, N. W., and Bradford, M. A.: Microbial formation of stable soil carbon is more efficient
790   from   belowground   than   aboveground   input,   Nat.   Geosci.,   12,   46–53,
791   https://doi.org/10.1038/s41561-018-0258-6, 2019.

792 Therneau, T., Atkinson, B.: Rpart: Recursive Partitioning and Regression Trees. R Package
793   Version 4.1-15, https://CRAN.R-project.org/package=rpart (last access: November 3,
794   2025).

Tsui, C. C., Liu, X. N., Guo, H. Y., and Chen, Z.S.: Effect of Sampling Density on Estimation of Regional Soil Organic Carbon Stock for Rural Soils in Taiwan, Geospatial Technology–Environmental and Social Applications, 35–53, https://doi.org/10.5772/64210, 2016.

Vaysse, K., and Lagacherie, P.: Evaluating digital soil mapping approaches for mapping GlobalSoilMap soil properties from legacy data in Languedoc-Roussillon (France), Geoderma Reg., 4, 20–30, https://doi.org/10.1016/j.geodrs.2014.11.003, 2015.

Vereecken, H., et al.: Soil hydrology in the Earth system, Nat. Rev. Earth Environ., 3, 573–587, https://doi.org/10.1038/s43017-022-00324-6, 2022.

Viaud, V., Angers, D. A., and Walter, C.: Toward landscape-scale modeling of soil organic matter dynamics in agroecosystems, Soil Sci. Soc. Am. J., 74, 1847–1860, https://doi.org/10.2136/sssaj2009.0412, 2010.

Villanueva, R. A. M., and Chen, Z. J.: ggplot2: Elegant Graphics for Data Analysis (2nd ed.), Measurement-Interdisciplinary Research and Perspectives, 17, 160-167, https://doi.org/10.1080/15366367.2019.1565254, 2019.

Wang, B., Waters, C., Orgill, S., Gary, J., Cowie, A., Clark, A., and Liu, D. L.: High resolution mapping of soil organic carbon stocks using remote sensing variables in the semi-arid rangelands of eastern Australia, Sci. Total Enviro., 630, 367–378, https://doi.org/10.1016/j.scitotenv.2018.02.204, 2018.

Wang, M. M., Zhang, S., Guo, X. W., Xiao, L. J., Yang, Y. H., Luo, Y. Q., Mishra, U., and Luo, Z. K.: Responses of soil organic carbon to climate extremes under warming across global biomes, Nat. Clim. Change, 14, 98–105, https://doi.org/10.1038/s41558-023-01874-3, 2023.

Wei, Y. C., Wang, M. M., Viscarra Rossel, R. A., Chen, H., and Luo, Z. K.: Extreme Climate as the Primary Control of Global Soil Organic Carbon Across Spatial Scales, Global Biogeochem. Cycles, 38, e2024GB008277, https://doi.org/10.1029/2024GB008200, 2024.

Wickham, H.: ggplot2: Elegant graphics for data analysis, 2nd ed. 2016. ed, Use R! Springer International Publishing: Imprint: Springer, Cham, https://doi.org/10.1007/978-3-319-24277-4, 2016.

Wiesmeier, M., Urbanski, L., Hobley, E., Lützow, M. V., Marin-Spiotta, E., Wesemael, B. V., Rabot, E., Ließ, M., Garcia-Franco, N., Wollschläger, U., Vogel, H. J., and Kögel-Knabner, I.: Soil organic carbon storage as a key function of soils–A review of drivers and indicators at various scales, Geoderma, 333, 149–162, https://doi.org/10.1016/j.geoderma.2018.07.026, 2019.

828 Zhang, G. Y., Luo, S., Jing, Z. W., Wei, S., and Ma, Y. H.: Evaluation and Forewarning
829   Management of Regional Resources and Environment Carrying Capacity: A Case Study
830   of   Hefei   City,   Anhui   Province,   China,   Sustainability,   12,   1637,
831   https://doi.org/10.3390/su12041637, 2020.

832 Zhu, Q., and Lin, H. S.: Comparing ordinary kriging and regression kriging for Soil properties
833   in contrasting landscapes, Pedosphere, 20, 594–606, https://doi.org/10.1016/S1002-
834   0160(10)60049-5, 2010.

835

836

837   **Table 1.** Environmental covariates.

Type of data	Environmental covariates	Soil forming factor	Type
Remote sensing	Normalized difference vegetation index (NDVI)	o; t	Q
Digital elevation model	Elevation	r	Q
	Slope	r	Q
	Aspect	r	Q
	Terrain ruggedness index (TRI)	r	Q
	Topographic wetness index (TWI)	r	Q
	Terrain position index (TPI)	r	Q
	Multiresolution Index of Valley Bottom Flatness (MrVBF)	r	Q
	Multiresolution Ridge Top Flatness (MrRTF)	r	Q
	Stream power index (SPI)	r	Q
	Curvature	r	Q
	Flow accumulation	r	Q
	R-value		Q
	K-value		Q
Climate	Mean annual temperature (MAT)	c; t	Q
	Total annual precipitation (TAP)	c; t	Q
Land cover	Land cover	o; t	C
Soil	Soil Order	s	C

838   s: soil, r: relief, c: climate, t: time, o: organism, Q: quantitative, C: categorical.

839

840   **Table 2.** Data partitioning rules and 5th/95th percentiles of leave-one-out validation residuals.

Class	Conditions	Residual percentile	
		P_5	P_{95}
1	Soil Order in Other	-1.08	0.80
2	Topographic Position Index ≤ -10.8889	-1.99	0.95
3	MAT > 17.09029, Topographic Position Index > -10.8889, Soil Order in Inceptisol, Entisol, Alfisol, Spodosol, Ultisol	-0.85	0.70
4	MAT ≤ 17.09029	-0.67	0.80

841

842

843 **Table 3.** Variance and coefficient of variance (CV) of the spatiotemporal distribution of SOC

844 stocks for various land uses in the two emission scenarios.

845

		2020				2050				2100			
		T	L	U	M	T	L	U	M	T	L	U	M
	Variance	6.45	0.66	1.35	5.11								
	CV(%)	44.3	32.3	30.7	32.5								
SSP1	Variance					5.52	0.35	0.85	4.37	8.24	0.76	1.56	6.45
2.6	CV(%)					50.4	29.8	33.9	36.0	51.3	33.5	39.2	36.4
SSP2	Variance					10.1	1.14	2.25	7.95	21.4	1.74	2.53	18.7
4.5	CV(%)					48.5	35.0	37.5	34.9	59.7	35.2	40.4	43.7

846 CV: coefficient of variance; T: total area; L: lowland regions; U: Upland regions; M: Mountainous regions.

847

848

849

850

851
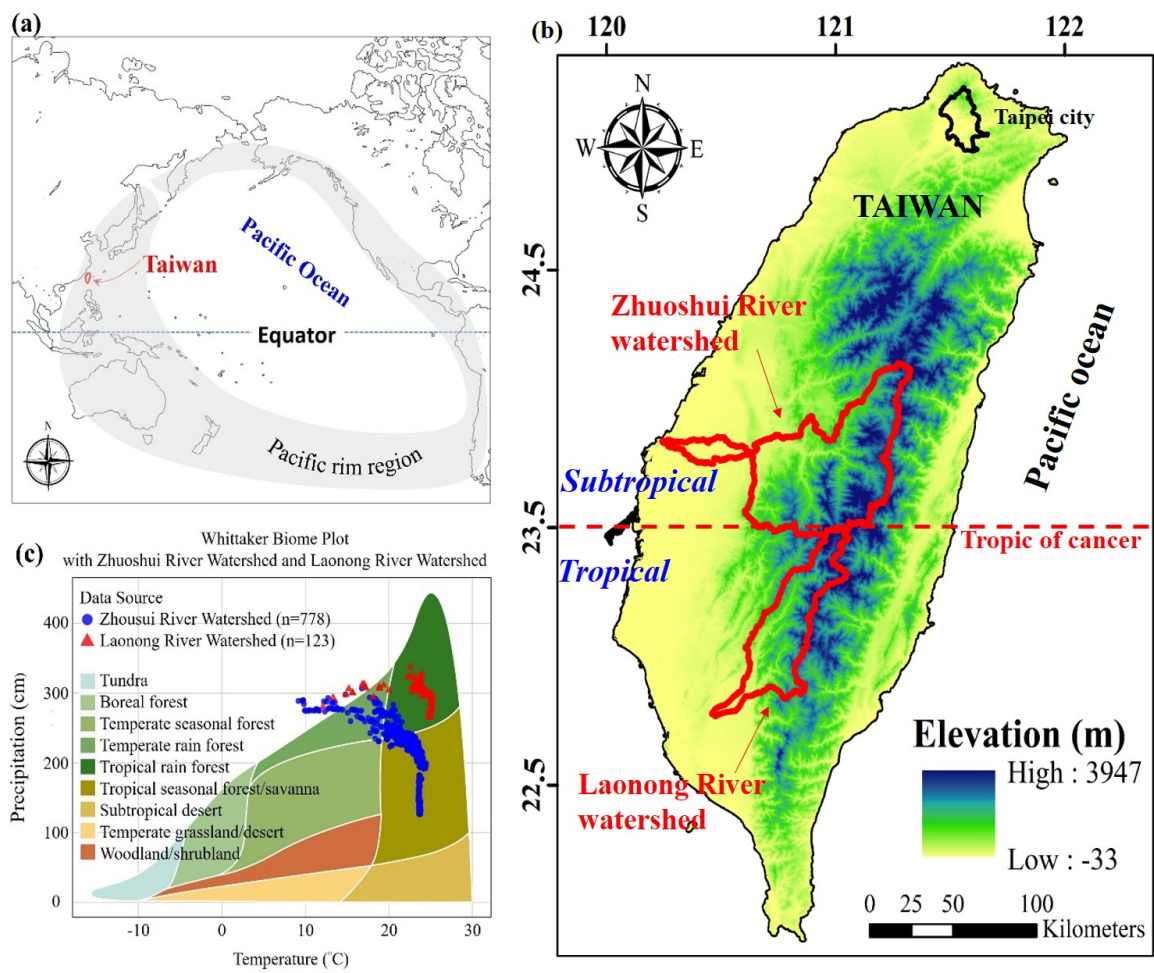
Fig. 1. Location of Taiwan in Pacific Ocean regions (a); location of Zhuoshui River watershed

(ZRW) and Laonong River watershed (LRW) in Taiwan; (c) Whittaker Biome Plot of ZRW and

LRW.
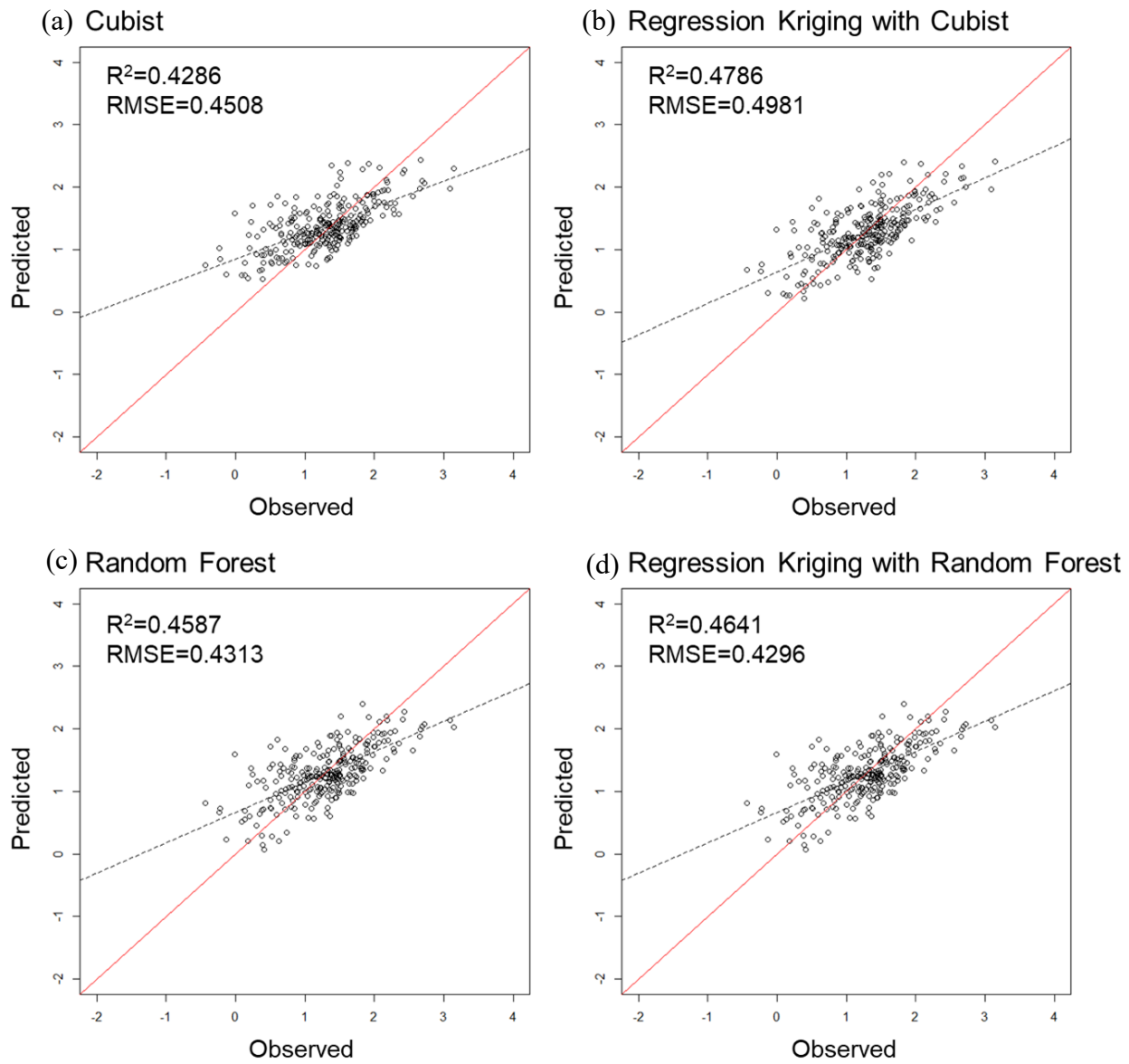
Fig. 2. Scatter plots of predicted versus observed soil organic carbon (SOC) stock in the topsoil (0–30 cm) where predictions were obtained on the basis of validation data and by using the (a) Cubist, (b) regression kriging (RK) with Cubist, (c) Random forest (RF), and (d) regression kriging with RF models. The *x*-axis represents the observed values, and the *y*-axis represents the predicted values. The solid line is the fitted line.

860
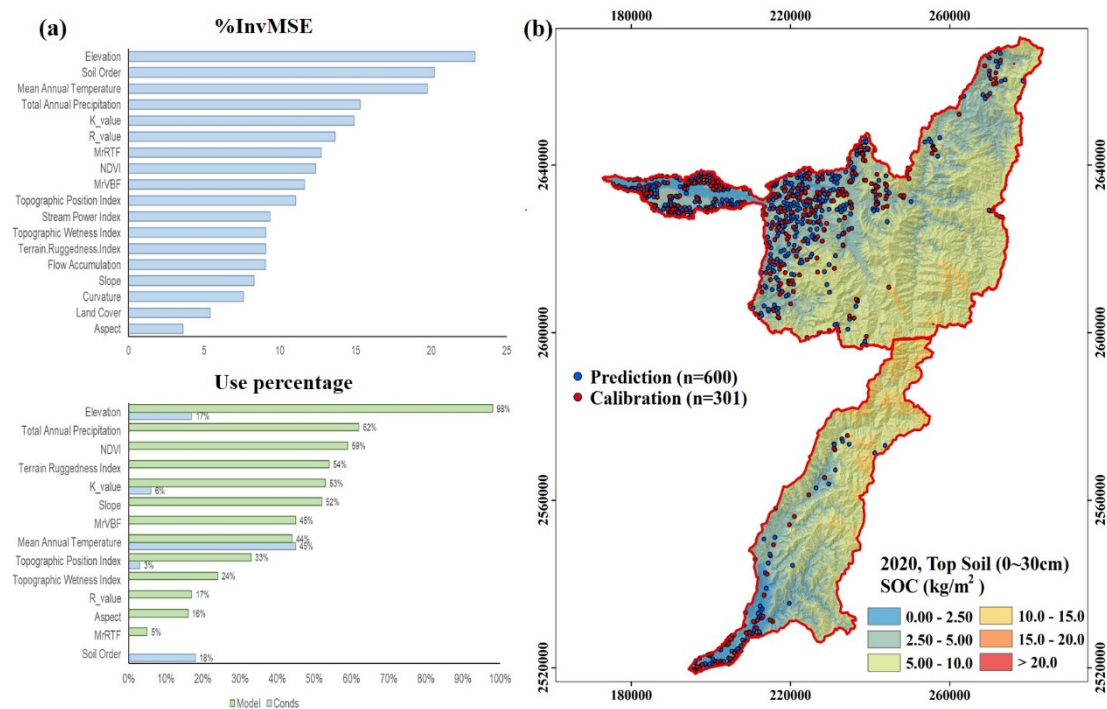
861   **Fig. 3.** (a) Variable importance of Random Forest and Cubist models for SOC stock in surface

862   soils (0–30 cm) and (b) predictive map of SOC stock in Zhuoshui River watershed and Laonong

863   River watershed.

864
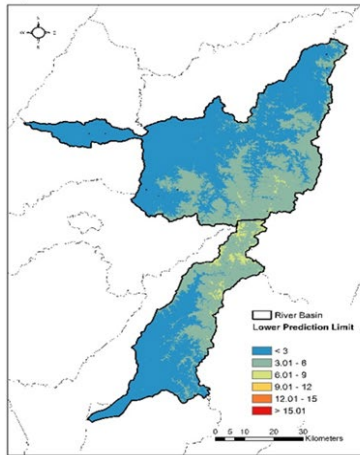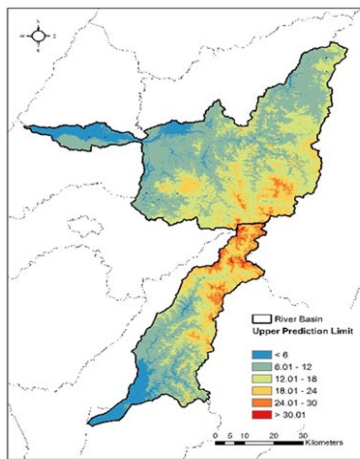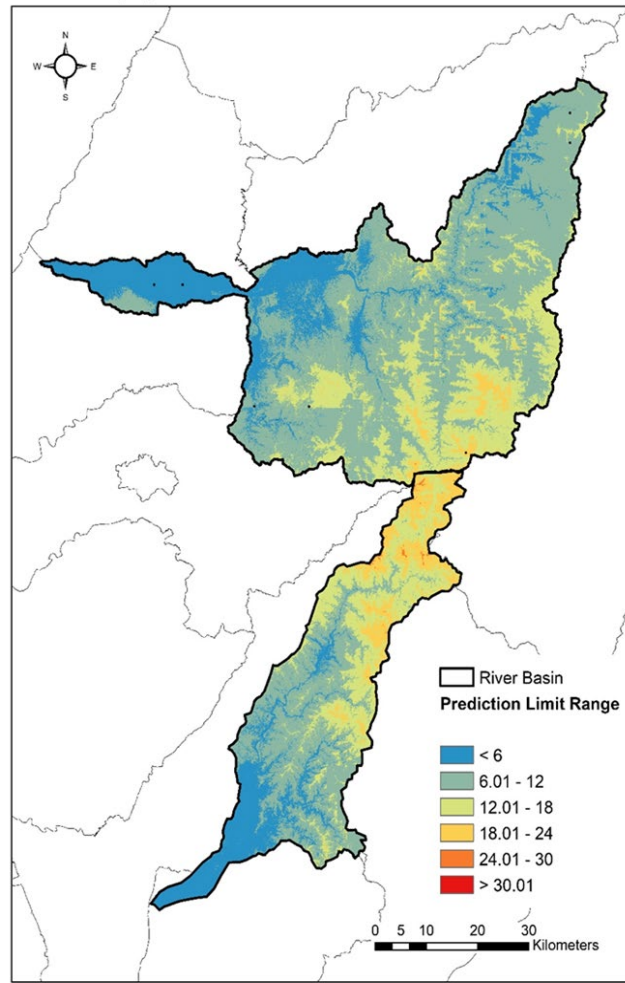
865 **Fig. 4.** Topsoil (0–30 cm) soil organic carbon (SOC) stock maps of the (a) 90% lower prediction

866 limit, (b) 90% upper prediction limit, and (c) prediction limit range derived using bootstrapping.

867
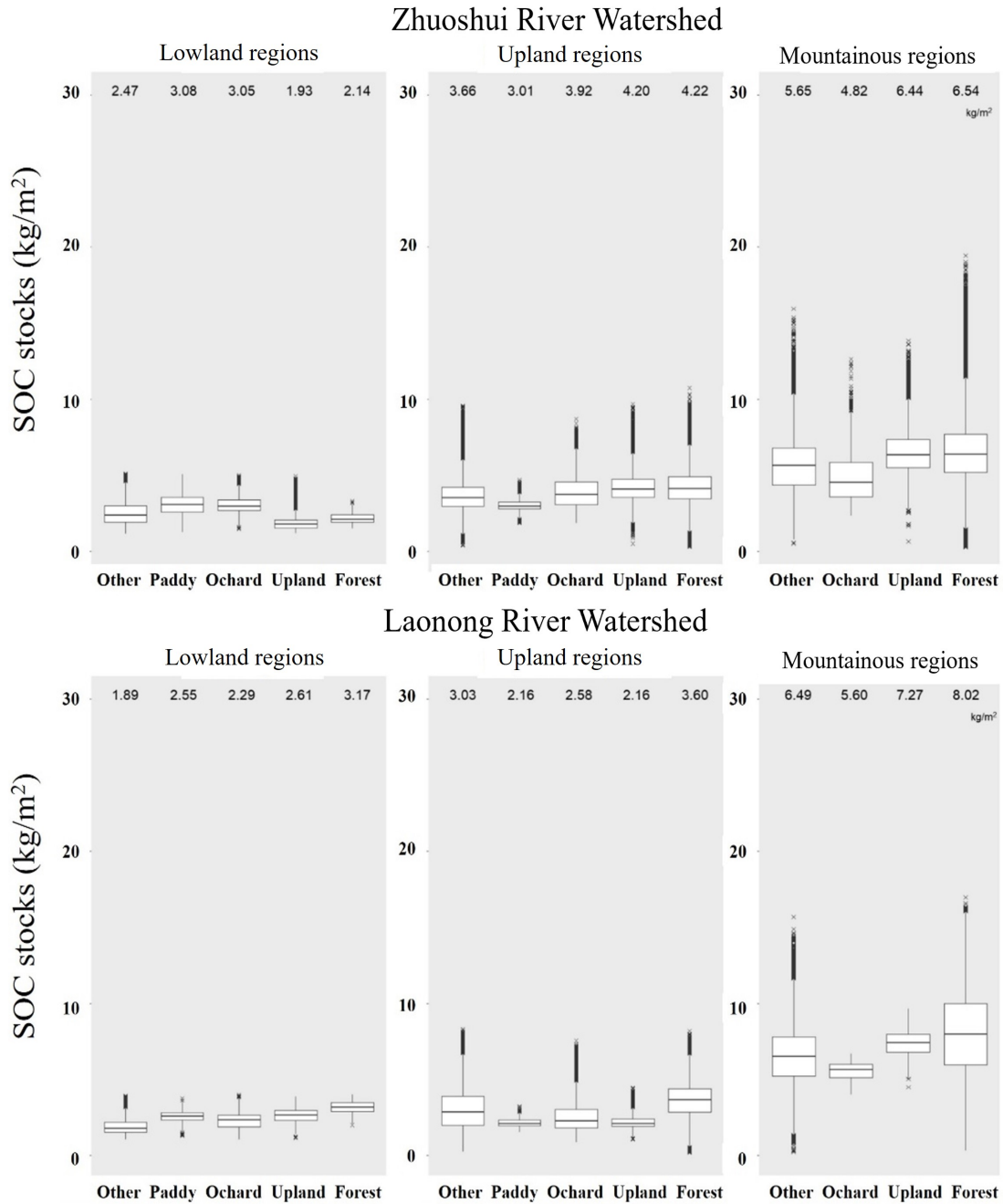
Fig. 5. Boxplots of topsoil (0–30 cm) soil organic carbon (SOC) stocks for various land cover: (left) lowland regions (<100 m in elevation), (middle) upland regions (100–1000 m in elevation), and (right) mountainous regions (>1000 m in elevation) at Zhuoshui River watershed and Laonong River watershed. The upland land cover represents the upland farming.

874
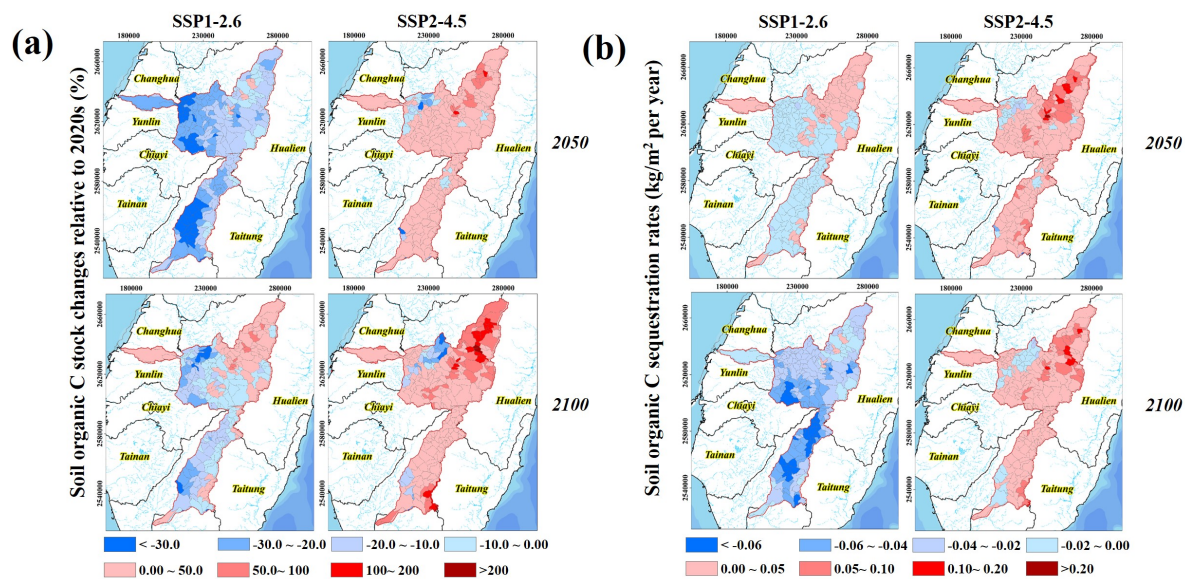
875 **Fig. 6.** Spatiotemporal predictions of (a) SOC stocks ($kg\,m^{-2}$) and (b) SOC sequestration rates

876 ($kg\,m^{-2}$ per year) relative to the 2020s under two emission scenarios. The mapping unit is sub-

877 catchments in Taiwan.
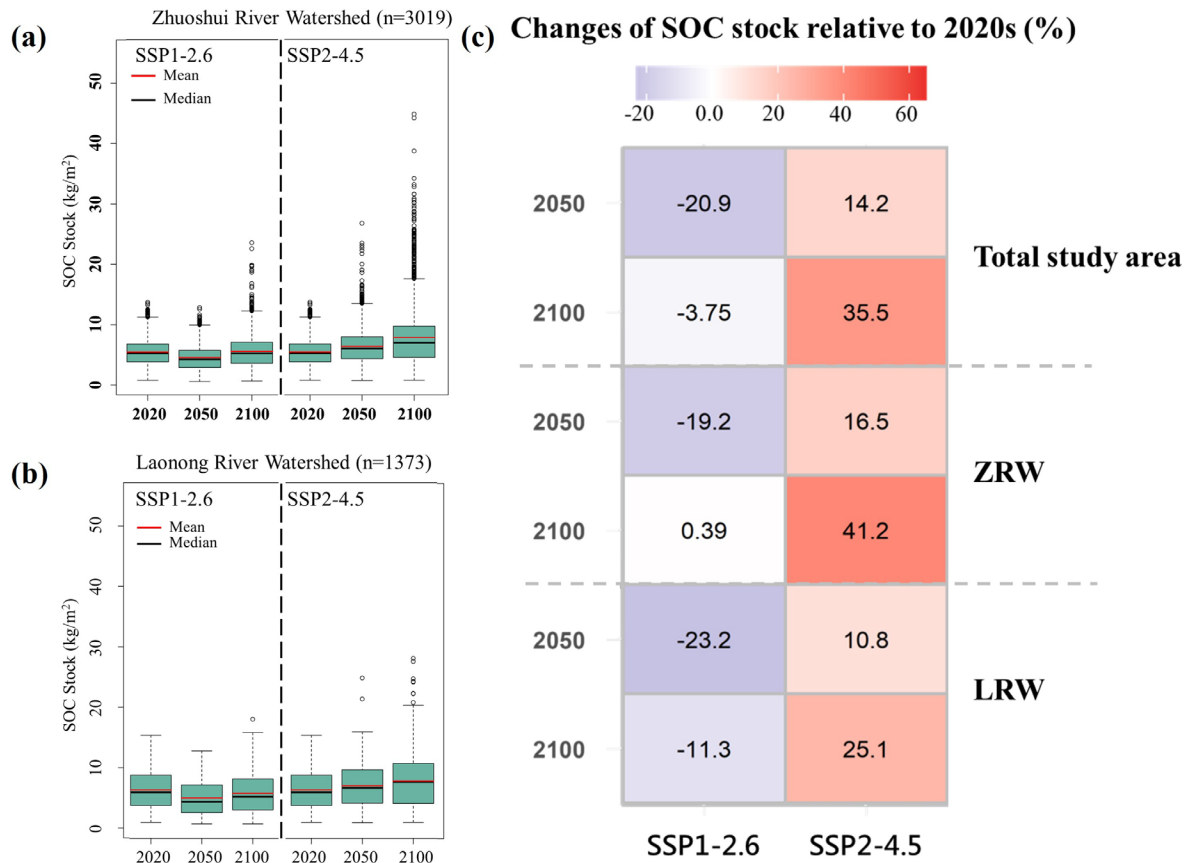
Fig. 7. Boxplots showing the temporal trends in predicted SOC stocks across two emission scenarios (SSP1-2.6 and SSP2-4.5) for 2020, 2050, and 2100 in (a) Zhuosui River watershed; and (b) Laonong River watershed, and (c) Increase in the ratio of SOC stocks relative to the 2020s in the ZRW and LRW for the two emission scenarios for 2050 and 2100.

884
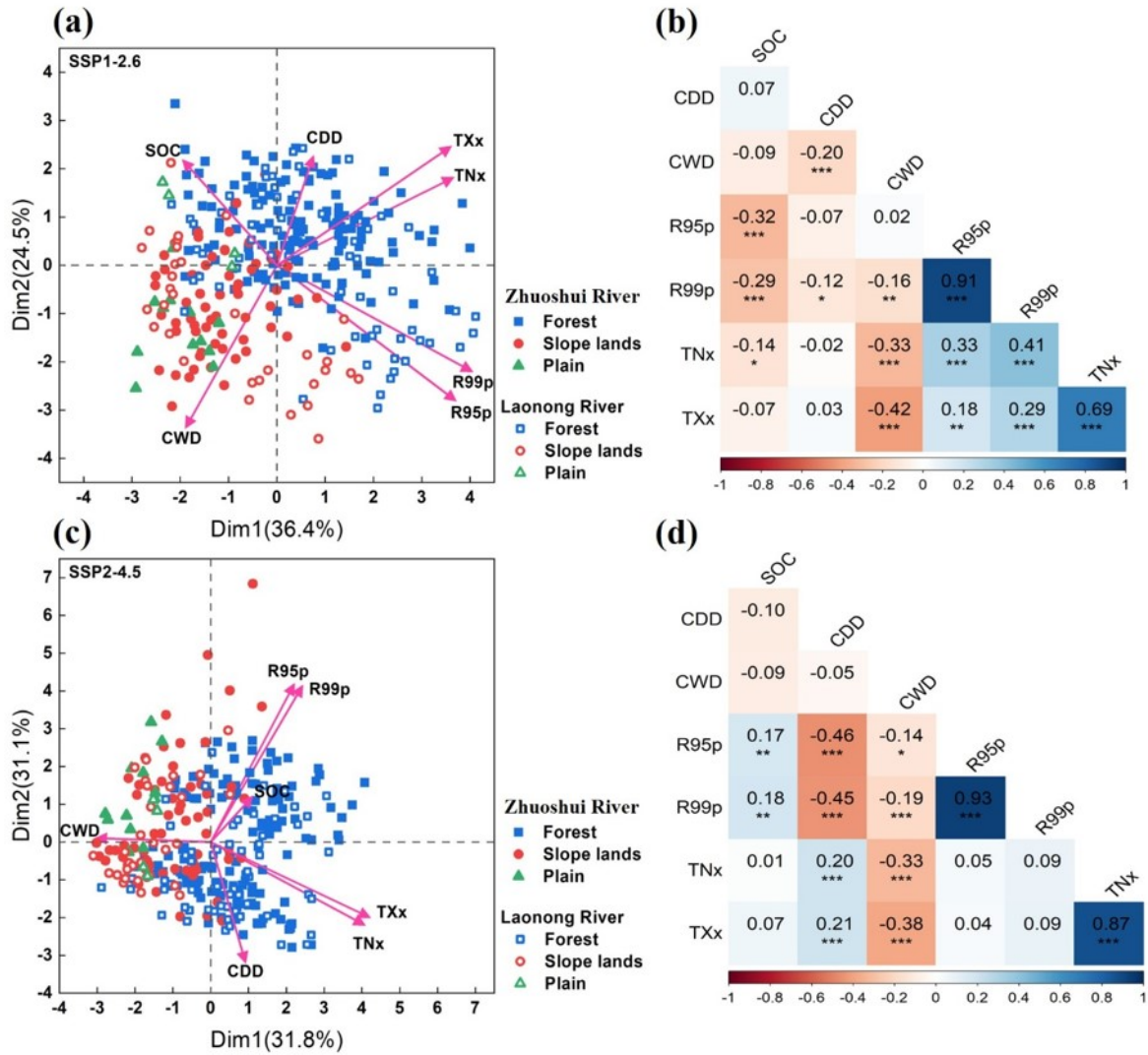
885 **Fig. 8.** Principal component analysis and Pearson's correlation coefficient of extreme climate

886 indices and SOC stocks: (a, b) and SSP1-2.6, (c, d) SSP2-4.5

887

888
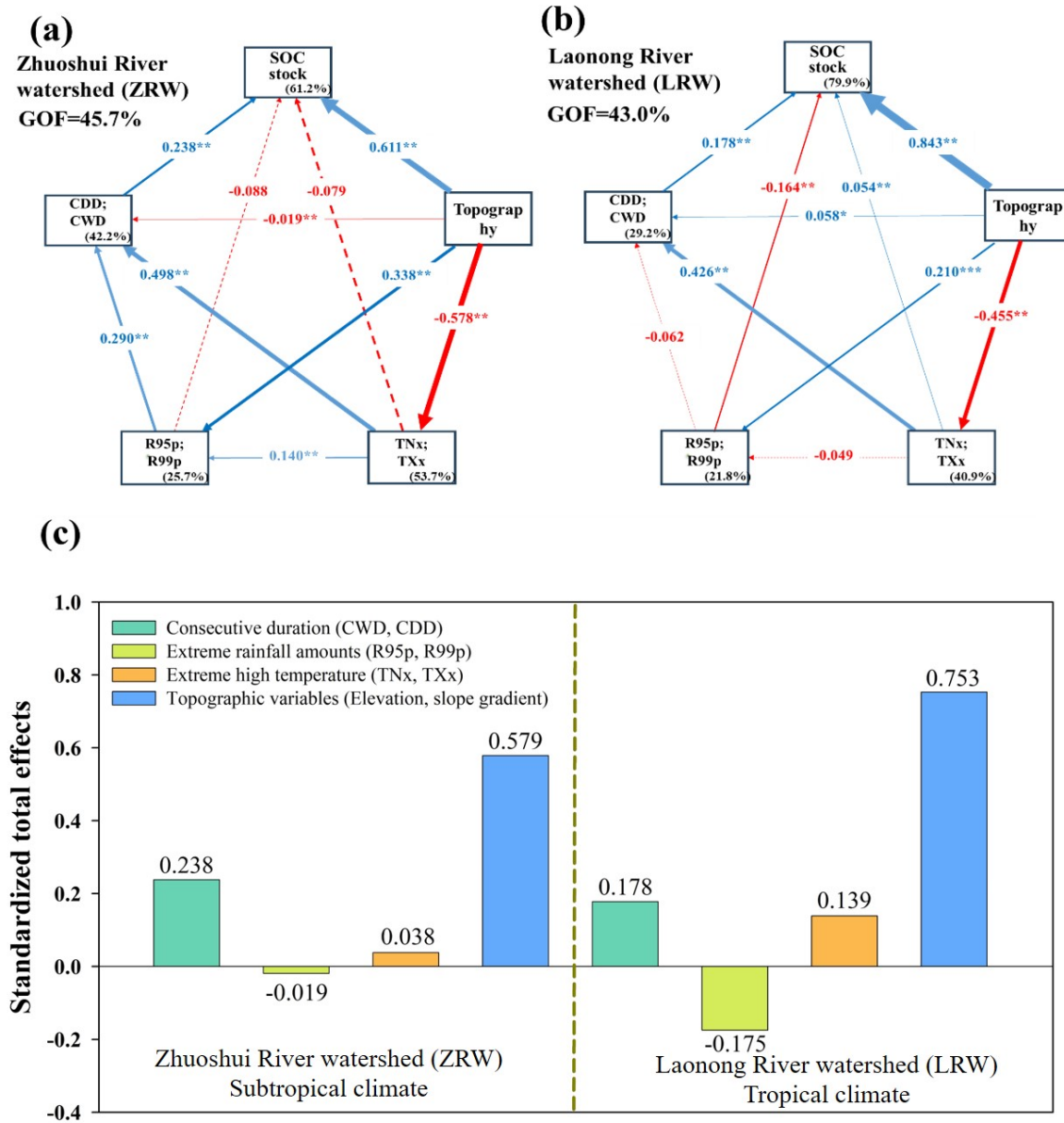
Fig. 9. Partial least squares path modeling (PLS-PM) analysis of the relationships among SOC

stocks, consecutive durations of extreme climatic events (CDD and CWD), extreme rainfall

amounts (R95p and R99p), extreme temperatures (TNx and TXx), and topographic variables

(elevation and slope gradient) (a) Zhuoshui River watershed; (b) Laonong River watershed; (c)

standardized total effects. Positive and negative effects are represented by blue and red arrows,

respectively. Path coefficients that do not significantly differ from zero are depicted as gray

dashed lines: $^*p < 0.05$ and $^{**}p < 0.01$. The percentages in the boxes represent the explanatory

power of the variables. The goodness-of-fit was used to assess the model.